JOURNAL OF COMPUTATIONAL PHYSICS 82, 362–397 (1989)

Higher Order Godunov Methods for General Systems of Hyperbolic Conservation Laws*

JOHN B. BELL, PHILLIP COLELLA, AND JOHN A. TRANGENSTEIN

Lawrence Livermore National Laboratory,
P.O. Box 808, Livermore, California 94550

Received September 15, 1987; revised May 13, 1988

We describe an extension of higher order Godunov methods to general systems of hyperbolic conservation laws. This extension allow the method to be applied to problems that are not strictly hyperbolic and exhibit local linear degeneracies in the wave fields. The method constructs an approximation of the Riemann problem from local wave information. A generalization of the Engquist–Osher flux for systems is then used to compute a numerical flux based on this approximation. This numerical flux replaces the Godunov numerical flux in the algorithm, thereby eliminating the need for a global Riemann problem solution. The additional modifications to the Godunov methodology that are needed to treat loss of strict hyperbolicity are described in detail. The method is applied to some simple model problems for which the global analytic structure is known. The method is also applied to the black-oil model for multiphase flow in petroleum reservoirs.

1. INTRODUCTION

Over the last 15 years, there has been an extensive effort in the development of conservative finite difference methods for computing discontinuous solutions to hyperbolic systems of conservation laws. The goal of this effort has been to develop viable numerical algorithms to solve problems in several specific applications, in particular, compressible fluid flow, plasma physics, and combustion. For reviews of various aspects of this work, see [1–3]. As a result of this effort, a set of heuristics for the design of "high resolution" methods for hyperbolic conservation laws has emerged. They can be summarized as follows.

(1) The numerical flux should consist of a hybridization of a flux for a first order method, and a flux for a higher order method. The first order method should be sufficiently dissipative so that, if it were used by itself, the numerical solution would converge to a weak solution satisfying appropriate entropy conditions. The rule by which the two fluxes are hybridized, known as the limiter, should include a sufficient amount of low-order flux at discontinuities and underresolved gradients

* This work was performed under the auspices of the U.S. Department of Energy by the Lawrence Livermore National Laboratory under Contract W-7405-Eng-48. Partial support under Contract W-7405-Eng-48 was provided by the Applied Mathematical Sciences Program of the Office of Energy Research and by the Air Force Office of Scientific Research under Grant AFOSR-ISSA-870016.

0021-9991/89 $3.00

to suppress oscillations and guarantee satisfaction of entropy conditions, while choosing the high order flux at almost all points where the solution is smooth.

(2) The underlying high order method should have low phase errors, either through the use of high order ($\geqslant$4th) spatial differencing or by using upstream-centered differencing [4].

(3) Additional dissipation is introduced as required in the neighborhood of strongly nonlinear discontinuities.

The above heuristics were arrived at by a combination of analysis of model problems, physical intuition, and numerical experiment. However, all of this work assumed, either explicitly or implicitly, two properties of the systems under consideration. First, the system should be strictly hyperbolic, with the linearized coefficient matrix possessing a complete set of linearly independent eigenvectors which were globally defined smooth functions of the dependent variables. Second, the system should satisfy the conditions set forth by Lax [5]; namely, each mode of wave propagation should be either genuinely nonlinear or linearly degenerate. Thus, the derivative of each eigenvalue along integral curves of the associated right eigenvector either never vanishes or is identically zero.

The extension of the above methodology to systems that are not strictly hyperbolic or violate the Lax conditions by having local linear degeneracies requires, at the very least, a careful reconsideration of the problem. The analytical information on which the methodology depends is either more complicated or simply unknown for more general systems of conservation laws. For example, the only schemes for nonlinear nonconvex scalar conservation laws in one space dimension that are known to converge to weak solutions satisfying appropriate entropy conditions are monotone schemes [6], which are only first-order accurate for smooth solutions. This is in contrast to the situation for convex scalar laws where it is possible to construct schemes which are second-order accurate for smooth solutions and converge to weak solutions satisfying the entropy condition. More generally, determining the correct entropy-satisfying discontinuities is much more complex for modes with local linear degeneracies, since it involves knowing the behavior of the wave speed at all points along the wave curve connecting the pre-wave and post-wave states. To make the same determination for genuinely nonlinear modes, the value of the wave speed is needed only at the pre-wave and post-wave states (see Liu [7]). Finally, the analytical structure of weak solutions is, in general, unknown in the neighborhood of a point where there is a loss of strict hyperbolicity. (For examples of the additional complexity exhibited by non-strictly hyperbolic systems, the reader can refer to Keyfitz and Kranzer [8] and Schaeffer and Shearer [9].)

In this paper, we extend a particular version of the high resolution methodology, viz., the higher order Godunov methods, to the case of general systems of hyperbolic conservation laws. We assume that in phase space the regions of local linear degeneracy or where strict hyperbolicity fail are codimension $\geqslant 1$, a condition which is satisfied by the applications that have been analyzed to date. In addition, it has been observed in specific model problems that the regions in space-time

where these conditions hold and the solution is not locally a constant are also of codimension $\geqslant 1$. Our strategy, then, is to detect those points in a calculation where the solution exhibits local linear degeneracy or non-strict hyperbolicity. At all other points, we use a variation on the standard Godunov methodology. At the exceptional points, the Godunov methodology is modified to provide a scheme that is stable and has sufficient dissipation so that an appropriate entropy condition is satisfied. The use of Godunov-type methodology is a particularly natural choice here, since the same characteristic information can be used both to construct the fluxes and to detect local linear degeneracy and non-strict hyperbolicity.

In the Godunov approach, the numerical fluxes are determined by computing a left and a right state at a cell edge, solving the Riemann problem for those two states and evaluating the flux along the appropriate ray. Even for applications in which the Riemann problem solutions are well understood analytically, approximations are often introduced for reasons of computational efficiency. See, for example, Roe [10] and Colella and Glaz [11]. In the present case, it is essential to introduce approximations to the Riemann problem solution, since the exact solutions are either unknown or prohibitively expensive to compute. The approximation we use here consists of two distinct parts. The first is a local model for the solution of the Riemann problem for strictly hyperbolic systems. Given an approximate solution in phase space (i.e., a collection of jumps, one for each family of waves which defines the jump across the wave of that family), we construct an interpolated wave speed along the wave paths connecting successive states. We use this local model to calculate an appropriate generalization for systems of the Engquist–Osher flux [12, 13] for scalar conservation laws. The extension we use is similar to that given by Osher and Solomon [14], but it does not require exact knowledge of the integral curves of the right eigenfields in phase space. The advantage of the Engquist–Osher approach is that it yields a flux formula which is at least as dissipative as the flux evaluated at the solution to the Riemann problem, with additional dissipation introduced only at transonic waves. At the same time, it is much less expensive than the corresponding Riemann-problem flux calculation, since it does not require determining which discontinuities satisfy the entropy condition. The second part of the algorithm consists of the modifications that are required when waves speeds coalesce and the system is no longer stricly hyperbolic. In particular, we discuss how the difficulties associated with coalescing wave speeds manifest themselves and how they can be detected. Then we describe the modification to the algorithm when loss of strict hyperbolicity is detected.

A review of the Engquist–Osher algorithm and a description of our numerical flux computation are presented in Section 2. The loss of strict hyperbolicity and the presence of local linear degeneracies necessitate additional modification to the higher order Godunov procedure; these are described in Section 3. The last two sections discuss numerical examples. The first of these discusses relatively simple model problems for which exact solutions are known. The latter describes an application of this methodology to a model for multiphase flow in porous media that includes mass transfer and compressibility effects.

2. Numerical Flux Computation

In this section we develop an approximate Riemann problem solver to compute a Godunov-type flux for systems that exhibit local linear degeneracies and loss of strict hyperbolicity. More precisely, we consider the system of conservation laws

$$U_t + F_x = 0, \tag{2.1}$$

where U is a vector of length K and F is a vector-valued function of U. We consider difference schemes of the form

$$U_j^{n+1} = U_j^n - \frac{\Delta t}{\Delta x}(F_{j+1/2} - F_{j-1/2}), \tag{2.2}$$

where U_j^n approximates the average value of the solution in cell Δ_j centered at x_j at time t^n and $F_{j+1/2}$ is the numerical flux. For the first-order Godunov method [15], the numerical flux is $F^G(U^L, U^R)$, which is defined to be the flux F evaluated at the state that propagates along the ray $x/t = 0$ in the Riemann problem solution for (2.1) with left state U^L and right state U^R. We note that the Godunov scheme only requires the flux evaluated at the state propagating with zero speed in the Riemann problem solution of the Riemann problem. For this reason our discussion focuses on the computation of this flux, not on obtaining a complete solution of the Riemann problem.

Scalar Conversation Laws

To fix ideas, we describe the basic algorithm for the scalar conservation law

$$u_t + f(u)_x = 0.$$

The method is based on the Engquist–Osher scheme for which the numerical flux is defined by an integral of the wave speed $a(u) = f'(u)$:

$$f^{EO}(u^L, u^R) = f(u^*) - \int_{u^L}^{u^*} \max(a(s), 0)\, ds + \int_{u^*}^{u^R} \min(a(s), 0)\, ds, \tag{2.3}$$

for any reference state u^*. The result is, of course, independent of u^*. The numerical flux given by (2.3) can be viewed as the flux at some reference state u^* plus a correction term given by the integral. Furthermore, the integral term contributes a dissipation term (possibly of zero magnitude) to the numerical flux. It is precisely this notion that Osher [6] exploits to show that the flux (2.3) can be written as the Godunov numerical flux plus a dissipation term. Furthermore, for convex flux functions, this dissipation is nonzero only for two states that describe a transonic compression; i.e., $f'(u^L) > 0$ and $f'(u^R) < 0$. This method for modifying the Godunov flux with some extra dissipation at transonic discontinuities provides the basis for the approximate Riemann problem solution described below.

We will approximate a using only values of first and second derivatives of f at u^L at u^R. The simplest approximation would be to linearly interpolate between

$a(u_L)$ and $a(u_R)$; however, the linear approximation, which corresponds to a quadratic approximation to the flux, is unable to represent inflection points in f. For this reason we approximate a on the interval between u^L and u^R by its Hermite cubic interpolant $\tilde{a}$. The cubic provides a local quartic model of the flux which can contain two inflection points. Before evaluating (2.3), we introduce an additional simplification to the approximation. We replace the cubic approximation $\tilde{a}$ by a piecewise linear approximation $\bar{a}$ in order to avoid finding zeroes of a cubic in the algorithm. First, we compute the extrema of $\tilde{a}$. The piecewise linear approximation $\bar{a}$ is then defined to be the piecewise linear interpolant of $\tilde{a}$ at u^L, u^R and the extrema.

We note that when the integrands in (2.3) are approximated, the flux is no longer independent of the reference state u^*. A variety of possible approximations to u^* are possible. We have used a simple upwind procedure based on the sign of

$$\bar{\sigma} \equiv \frac{f(u^L) - f(u^R)}{u^L - u^R}.$$

We take $u^* = u^L$ if $\bar{\sigma} \geqslant 0$; otherwise we take $u^* = u^R$. (This type of secant condition was used in a more general form by Murman and Cole [16] to choose an upwind state for the transonic small-disturbance equation.) Of course, more sophisticated approaches for determining the reference state can easily be incorporated into the algorithm.

Using the above definition of the reference state, we evaluate (2.3) with a approximated by $\bar{a}$. Thus, the approximate flux for scalar conservation laws is

$$f^s(u^L, u^R) = f(u^*) - \int_{u^L}^{u^*} \max(\bar{a}(s), 0)\, ds + \int_{u^*}^{u^R} \min(\bar{a}(s), 0)\, ds. \tag{2.4}$$

We note that this form ensures that the numerical flux is the reference flux plus a dissipation term. In particular,

$$f^s = f(u^*) - [\alpha^+ \beta + \alpha^- (1 - \beta)](u^R - u^L), \tag{2.5}$$

where

$$\alpha^+ = \frac{1}{(u^* - u^L)} \int_{u^L}^{u^*} \max(\bar{a}(s), 0)\, ds,$$

$$\alpha^- = \frac{1}{(u^R - u^*)} \int_{u^*}^{u^R} |\min(\bar{a}(s), 0)|\, ds,$$

and

$$\beta = \frac{u^* - u^L}{u^R - u^L}.$$

Both of the terms α^+ and α^- are nonnegative and $0 \leqslant \beta \leqslant 1$ for u^* between u^L and u^R; thus, the additional term represents a dissipation (possibly of zero magnitude).

The motivation for using a local model comes from our experience in the case of a convex flux. For a convex flux, the only case for which $f^{EO} \neq f(u^*)$ is if $a(u^L)\, a(u^R) < 0$. For that case, it suffices to approximate $a(u)$ as a linear function of u in (2.4). The dissipative term so introduced, while not identical to that implicitly introduced by the exact Engquist–Osher flux, is nonzero for all cases where the latter is nonzero and sufficient to ensure that any discontinuities computed satisfy the appropriate entropy condition. For the case of a flux with isolated extrema in $a(u)$, the appropriate analog of a local linear representation of $a(u)$ is to represent a as a polynomial of degree $\geqslant 2$, which is sufficient to represent a single isolated extremum in a. (We use a cubic, since we evaluate da/du at both the left and the right state.) Thus if $u^R - u^L$ is sufficiently small, our approximate flux will add to $f(u^*)$ a dissipation which is nonzero whenever the analogous dissipation for f^{EO} is nonzero. In practice, we have found that the procedure given here produces discontinuities satisfying the appropriate entropy conditions for large amplitude jumps, provided that we add a suitable quadratic viscosity to the flux, i.e., $f^s \to f^s + \eta(u^L - u^R)$, $\eta = O(u^L - u^R)$. To understand why this should be the case, let δ be the maximum jump for which our local model procedures a flux which is sufficiently close to that given by the Engquist–Osher flux in the sense described above, and assume that $\eta \approx C\,|u^L - u^R|/\delta$. Then there are two cases. When the magnitude of the jump is less than δ, then the principal dissipation mechanism is that of the Engquist–Osher flux. In the case when the magnitude of the jump is much larger than delta, then the explicit artificial viscosity acts like a linear viscous term. In both cases, the dissipation is sufficient to enforce the entropy condition. Furthermore, the fact that the explicit viscosity is quadratic in the jump will enable us extend the overall approach to be second order accurate for smooth solutions.

Systems

Now we generalize the numerical flux approximation (2.4) to stricly hyperbolic systems of equations. Our approximation procedure for systems breaks the flux computation into two distinct pieces. First, we construct a path from U^L to U^R that approximates the phase-space solution of the Riemann problem. The phase-space solution can be constructed without regard to physical (x, t) space considerations. An approximation to the wave speeds along the phase-space path establishes a physical-space representation of the Riemann-problem solution and provides the information needed to compute the flux using a system analog of (2.4).

To make precise the notion of a phase space solution we must first describe the structure of the Riemann problem for strictly hyperbolic conservation laws. (For a more detailed description see Lax [17]). For such a system the solution of the Riemann problem consists of up to K distinct waves progressing from U^L to U^R separated by $K-1$ intermediate states. We will refer to the slowest (minimum velocity) wave as a 1-wave and the fastest (maximum velocity) wave as an K-wave, etc. The solution of the Riemann problem is constructed in phase space by

following "wave curves." For any state U, we define the kth wave curve through U to be the set of all states that can be connected to U with a k-wave. The Riemann problem solution in phase space is thus a collection of state transitions

$$U^{\mathrm{L}} = U_0 \to U_1 \to \cdots \to U_{K-1} \to U_K = U^{\mathrm{R}},$$

where the transition from U_{k-1} to U_k occurs along some arc Γ_k of the kth wave curve.

In the limit of small amplitude jumps

$$U_k - U_{k-1} = \alpha_k r_k + O(|U^{\mathrm{R}} - U^{\mathrm{L}}|^2),$$

where r_k is the right eigenvector of $DF(U^{\mathrm{L}})$ corresponding to the kth eigenvalue (with ordering $\lambda_1 < \lambda_2 < \cdots < \lambda_m$). The amplitude α_k is, to leading order, the coefficient of the expansion of $U^{\mathrm{R}} - U^{\mathrm{L}}$ in terms of the r_k,

$$U^{\mathrm{R}} - U^{\mathrm{L}} = \sum_{k=1}^{K} \alpha_k r_k + O(|U^{\mathrm{R}} - U^{\mathrm{L}}|^2).$$

Analogously, in the general case of finite amplitude jumps, the phase-space solution of the Riemann problem takes the form

$$\mathrm{U}^{\mathrm{R}} - U^{\mathrm{L}} = \sum_{k=1}^{K} \alpha_k R_k,$$

where R_k is a "generalized" eigenvector that represents the net change along Γ_k, normalized to be of unit length.

From this analytic perspective the approximate phase-space solution is a decomposition of the jump from U^{L} to U^{R} into K jumps corresponding to each of the wave modes. To approximate this decomposition we need a set of linearly independent $\bar{R}^k$ along with associated approximations to the wave curves $\bar{\Gamma}_k$ that approximate the Γ_k. If we expand $U^{\mathrm{R}} - U^{\mathrm{L}}$ in terms of the $\bar{R}_k$'s we obtain

$$U^{\mathrm{R}} - U^{\mathrm{L}} = \sum_{k=1}^{K} \bar{\alpha}_k \bar{R}_k, \tag{2.6}$$

where $\bar{\alpha}_k$ approximates α_k. For the computations reported here, we have used a particularly simple approximate phase space solution. In particular, we let $U^e = 1/2(U^{\mathrm{L}} + U^{\mathrm{R}})$. We then let $\bar{R}_k = r_k(U^e)$, the kth right eigenvector of DF at U^e corresponding to wave speed λ_k^e. (Because of the subsequent approximations, the path $\bar{\Gamma}_k$ is not explicitly needed in the algorithm. For convenience, we will, however, define the path to be the line segment connecting $\bar{U}_{k-1}$ and $\bar{U}_k$.) For other problem areas having "stronger" nonlinearities such as elastic-plastic flow or high-speed multiphase flow a more elaborate approach may be merited. In any case, the flux computation is independent of the technique used to obtain the phase-space solution.

We now turn to the problem of computing a numerical flux. Our goal is to develop an analog of Eq. (2.4) for systems. As was the case for scalars, the numerical flux will be written as the flux at some reference state plus an integral correction term. Following Harten and Lax [18] we define a mean speed

$$\bar{\sigma} = \frac{(F(U^{\mathrm{L}}) - F(U^{\mathrm{R}})) \cdot (U^{\mathrm{L}} - U^{\mathrm{R}})}{\|U^{\mathrm{L}} - U^{\mathrm{R}}\|^2}.$$

We then define the reference state $U^* = U^{\mathrm{L}}$ if $\bar{\sigma} \geqslant 0$; otherwise $U^* = U^{\mathrm{R}}$. This definition has proven adequate for porous media flow. In some applications, one of the intermediate states

$$\bar{U}_{\bar{k}} = U^{\mathrm{L}} + \sum_{k=1}^{\bar{k}} \bar{\alpha}_k \bar{R}_k$$

may be a more appropriate choice. If intermediate states are used for computing the reference flux, some caution is required when the system exhibits loss of strict hyperbolicity; see discussion in the next subsection. For clarity of exposition we will assume that the reference state is U^{L} for the remainder of the section. We also assume that the $\bar{R}_k$'s have been oriented so that the α_k are positive.

For the system case, there are K contributions to the integral term corresponding to each term in the expansion (2.6). The kth term in the expansion corresponds to a k wave. Thus, a natural analog of (2.3) for systems would be

$$F(U^{\mathrm{L}}) + \sum_{k=1}^{K} \int_{\Gamma_k} DF\, \tau_k \chi_k \, ds, \tag{2.7}$$

where χ_k is the characteristic function of the set $\{U\colon \lambda_k(U) \leqslant 0\}$, τ_k is the tangent to Γ_k, and s parametrizes Γ_k. If we substitute the approximate phase-space solution for the true phase-space solution in (2.7) we obtain

$$F(U^{\mathrm{L}}) + \sum_{k=1}^{K} \int_{\bar{\Gamma}_k} DF\, \bar{\tau}_k \chi_k \, ds, \tag{2.8}$$

where $\bar{\tau}_k$ is the tangent to $\bar{\Gamma}_k$.

To compute the flux we want to develop an approximation to (2.8). Some care must be taken in constructing the approximation so that the correction term has a dissipative form. The first step in this process is to construct an approximation to the kth wave speed along the line segment $\bar{\Gamma}_k$ from U_{k-1} to U_k. The procedure is analogous to the scalar procedure. We let λ_k^{L} and λ_k^{R} denote the eigenvalues at U^{L} and U^{R} arranged in increasing order. At U^{L} and U^{R} we also compute the structure coefficients defined as

$$\kappa_{kl}^{\mathrm{L,R}} \equiv (\nabla_U \lambda_k)^{\mathrm{L,R}} \cdot \bar{R}_l.$$

We then use κ_{kk}^{L} and κ_{kk}^{R} to provide the second derivative information needed to compute the cubic approximation $\tilde{\lambda}_k$ of λ_k along $\bar{\Gamma}_k$. The approximation $\tilde{\lambda}_k$ is then modified, as before, to obtain a piecewise linear approximation $\bar{\lambda}_k$. We note that by using wave speeds at U^{L} and U^{R} to model the wave speed along $\bar{\Gamma}_k$ we avoid additional characteristic analyses and potential problems arising from errors in the phase-space solution. Also, this approximation is correct to second order in the jump so that the accuracy required for overall second-order accuracy of the method is preserved.

The next step in the process is to approximate $DF\,\bar{\tau}_k$ in terms of the approximate wave speed. It is known (see Lax [5] and Liu [7]) that along the wave curves

$$DF\,\tau_k = \lambda_k r_k + O(U^{\mathrm{R}} - U^{\mathrm{L}})^2.$$

This leads to the approximation of (2.8) by

$$F^S(U^{\mathrm{L}}, U^{\mathrm{R}}) = F(U^{\mathrm{L}}) + \sum_{k=1}^{K} \left(\int_0^{\bar{\alpha}_k} \min(\bar{\lambda}_k, 0)\, d\alpha \right) \cdot \bar{R}_k. \tag{2.9}$$

Equation (2.9) is the approximation flux formula (when the reference state is U^{L}). A system analog of (2.5) shows that the integral terms in (2.9) add a nonnegative dissipation to each of the characteristic modes in the expansion of $U^{\mathrm{R}} - U^{\mathrm{L}}$.

Loss of Strict Hyperbolicity

In this subsection we examine the necessary modifications to the approximate Riemann problem solution described earlier in this section when there is a loss of strict hyperbolicity. There are two possibilities when wave speeds coalesce. Either the Jacobian of the flux DF can be diagonalized or it will contain a nontrivial Jordan block. The procedures outlined below are designed with the eigenvector deficiency case in mind as this is the case in which the construction above clearly breaks down. We will, in fact, describe the algorithm in terms of the detection of eigenvector deficiencies and their treatment. However, we do not distinguish between these two possible cases in the algorithm. This is essentially a safety precaution that avoids potential difficulties associated with inconsistencies in the definition of the eigenstructure even when the system is diagonalizable. Such inconsistencies can arise because, in the general case, there is not necessarily a global ordering of the wave speeds that will define smooth right eigenvectors when wave speeds coincide. Furthermore, the eigenstructure may not vary smoothly in a neighborhood of a point where strict hyperbolicity fails.

In actual computations it is rare to encounter points where wavespeeds are numerically equal. The real numerical difficulties originate from the approximate phase-space solution of the Riemann problem in which we compute the eigenvectors that will be used to expand $U^{\mathrm{R}} - U^{\mathrm{L}}$. In a neighborhood of the eigenvector deficiency two of the eigenvectors become nearly parallel. This leads to large expansion coefficients in (2.6) that cannot be uniformly bounded analytically in terms of $U^{\mathrm{R}} - U^{\mathrm{L}}$. The phase-space approximation is not reasonable and its use in

conjunction with the flux computation (2.9) can potentially introduce instabilities into the numerical method.

The first step in dealing with eigenvector deficiencies in the algorithm is to detect them. The detection algorithm is based on a pairwise criterion that estimates whether or not it is possible for two of the wave speeds to coincide in the vicinity of the phase-space solution of the Riemann problem. Specifically, if

$$|\lambda_l^e - \lambda_m^e| < c \sum_{k=1}^{K} \bar{\alpha}_k |\kappa_{lk} - \kappa_{mk}| \tag{2.10}$$

then we assume that λ_l^e and λ_m^e may be involved in an eigenvector deficiency and we apply the modifications discussed below. In all of the computations presented in this paper we have used $c = 0.1$.

When we detect that two wave speeds may coalesce we only modify the treatment of the two particular wave families involved; the remaining wave families are treated in the same manner as before. When more than two speeds are involved the requisite changes are a natural of extension of the procedure; consequently, we discuss only the two-mode case. In particular, we assume that the eigenvalues λ_l^e and λ_m^e satisfy (2.10). As before, we assume that the reference state is U^{L}. The modification to the flux computation is motivated by the assumption that (2.10) is satisfied because we are near an eigenvector deficiency so that $\bar{R}_l$ and $\bar{R}_m$ are nearly parallel. This leads to ill-conditioning of the matrix associated with the expansion (2.6), consequently this expansion cannot be used. Furthermore, we also assume that the structure coefficients κ_{lk} and κ_{mk} are not reliable.

The actual modifications to the flux computation depend on whether the eigenvector deficiency is associated with a change in the sign of the wave speeds during the transition from U^{L} to U^{R}. To this end we let

$$\lambda_{lm}^{\min} = \min(\lambda_l^{\mathrm{L}}, \lambda_l^{\mathrm{R}}, \lambda_m^{\mathrm{L}}, \lambda_m^{\mathrm{R}})$$

and

$$\lambda_{lm}^{\max} = \max(\lambda_l^{\mathrm{L}}, \lambda_l^{\mathrm{R}}, \lambda_m^{\mathrm{L}}, \lambda_m^{\mathrm{R}}).$$

If $\lambda_{lm}^{\lim}$ and $\lambda_{lm}^{\max}$ are of the same sign, then we assume that the deficiency is not associated with a transonic wave. In this case we collapse $\bar{\alpha}_l \bar{R}_l + \bar{\alpha}_m \bar{R}_m$ into a single jump by defining

$$\bar{R}_{lm} = \frac{\bar{\alpha}_l \bar{R}_l + \bar{\alpha}_m \bar{R}_m}{\|\bar{\alpha}_l \bar{R}_l + \bar{\alpha}_m \bar{R}_m\|}; \qquad \bar{\alpha}_{lm} = \|\bar{\alpha}_l \bar{R}_l + \bar{\alpha}_m \bar{R}_m\|$$

and define the flux

$$F^S(U^{\mathrm{L}}, U^{\mathrm{R}}) = F(U^{\mathrm{L}}) + \left(\int_0^{\bar{\alpha}_{lm}} \min(\bar{\lambda}_{lm}, 0)\, d\alpha \right) \bar{R}_{lm} + \sum_{k \neq l,m} \left(\int_0^{\bar{\alpha}_k} \min(\bar{\lambda}_k, 0)\, d\alpha \right) \bar{R}_k, \tag{2.11}$$

where $\bar{\lambda}_{lm}$ is a linear function such that

$$\bar{\lambda}_{lm}(0) = \max(\lambda_l^{\mathrm{L}}, \lambda_m^{\mathrm{L}})$$

and

$$\bar{\lambda}_{lm}(\bar{\alpha}_{lm}) = \min(\lambda_l^{\mathrm{R}}, \lambda_m^{\mathrm{R}}).$$

This choice of $\bar{\lambda}$ assumes the wave is maximally compressive, which incorporates a judicious amount of additional dissipation because of the Engquist–Osher formalism. Note that this differs from simple upwinding for the case in which $\bar{R}_{lm}\bar{\lambda}_{lm} < 0$.

The only case that remains is when $\lambda^{\min}$ and $\lambda^{\max}$ are of opposite signs. When this occurs, we replace the integral correction term by a dissipative term similar to that which is incorporated into Rusanov's scheme [19]. More precisely, in this case the numerical flux is

$$F^S(U^{\mathrm{L}}, U^{\mathrm{R}}) = F(U^{\mathrm{L}}) - \tfrac{1}{2}\nu\bar{\alpha}_{lm}\bar{R}_{lm} + \sum_{k \neq l,m} \left(\int_0^{\bar{\alpha}_k} \min(\bar{\lambda}_k, 0)\, d\alpha \right) \bar{R}_k, \qquad (2.12)$$

where $\nu = \max(|\lambda_l^{\mathrm{L}}|, |\lambda_m^{\mathrm{L}}|, |\lambda_l^{\mathrm{R}}|, |\lambda_m^{\mathrm{R}}|)$.

3. Higher Order Considerations

If we use the numerical flux defined by (2.9) along with the modifications for non-strict hyperbolicity (2.11) and (2.12) to replace the Godunov flux in (2.2), we would have a formally first-order numerical approximation to the system of conservation laws (2.1). Our goal in this section is to construct a higher order Godunov method that is suitable for general systems of conservation laws. Our basic approach follows the development given by Colella [20] for systems satisfying the Lax hypotheses. Although we will give a complete description of the algorithm, our discussion will focus on the modifications required for general systems. Roughly speaking, the basis for the higher order method is the observation that if the left and right states used to compute the flux $F_{j+1/2}$ were second-order approximations to U at $x_{j+1/2}$, $t^{n+1/2}$, then the difference scheme defined by (2.2) would be a formally second-order approximation. The procedure used to compute these second-order approximations is a two step process. First, we construct a linear approximation to U at time t^n within each grid cell. The linear approximation is monotonized to prevent oscillations from being introduced near discontinuities in the solution. The quasilinear form of the equation is then used to extrapolate to cell interfaces at $t^{n+1/2}$.

We begin by describing the reconstruction process, which defines a linear profile for U within each grid cell. This approximation preserves cell averages U_j^n so we

need only to compute an approximation to the slope. We define a monotonized, centered-difference approximation

$$\frac{\Delta U_j}{\Delta x} \approx \left.\frac{\partial U}{\partial x}\right|_{x=x_j}. \tag{3.1}$$

To calculate ΔU_j, we first define the expansions

$$\begin{aligned} \tfrac{1}{2}(U_{j+1} - U_{j-1}) &= \sum \alpha_k^c r_k \\ (U_{j+1} - U_j) &= \sum \alpha_k^r r_k \\ (U_j - U_{j-1}) &= \sum \alpha_k^l r_k, \end{aligned} \tag{3.2}$$

where the r_k are the right eigenvectors of $DF(U_j)$. (In the unlikely case of a numerical eigenvector deficiency a complete set of right eigenvectors is defined by setting to zero off-diagonal terms in the Jordan form of the matrix; however, the entire jump corresponding to the nontrivial Jordan block will be treated as a single jump so that this treatment of the deficient case is solely a matter of implementation convenience.) The basic algorithm used by Colella [20] then defines

$$\Delta U = \sum \alpha_k r_k, \tag{3.3}$$

where

$$\alpha_k = \begin{cases} \min(|\alpha_k^c|, \gamma|\alpha_k^l|, \gamma|\alpha_k^r|) \times \operatorname{sign}(\alpha_k^c) & \text{if } \alpha_k^r \alpha_k^l > 0 \\ 0, & \text{otherwise.} \end{cases}$$

This form of "limiting" the slopes with $\gamma = 2$ is adequate for strictly hyperbolic systems that are genuinely nonlinear; however, additional limiting is required near local linear degeneracies and when eigenvector deficiencies are detected among the r_k.

A sufficient modification when a local linear degeneracy is detected is to set $\gamma = 1$ in (3.3). The reduction of γ has the effect of adding additional dissipation in the vicinity of the shock for composite shock-rarefaction waves. This additional dissipation is needed to ensure that the shock does not become too sharp and thereby produce a violation of the Oleinik–Liu entropy condition. (See Bell and Shubin [21]) for a discussion of a scalar example where this type of modification is required to obtain entropy satisfying shock waves.) Local linear degeneracies are detected using the structural coefficients $\kappa_{kl,j} = ((\nabla\lambda_k) \cdot r_l)_j$ (where the j subscript refers to the jth grid cell). In particular, if

$$\kappa_{kk,j}\kappa_{kk,j+1} < 0 \qquad \text{or} \qquad \kappa_{kk,j}\kappa_{kk,j-1} < 0$$

then we set $\gamma = 1$ when limiting $\alpha_{k,j}^c$.

The numerical difficulties associated with eigenvector deficiencies are considerably more serious. The issues here are the same as those that arise in the flux computation. Near an eigenvector deficiency the right eigenvectors used in the expansions in (3.2) become nearly parallel. There is an associated loss of any uniform bounds on the α^c in (3.2) in terms of the jump resulting in unreliable expansion coefficients. Eigenvector deficiencies in the slope computation are detected using an analog of (2.10); namely, if

$$|\lambda_l - \lambda_m| < c \sum_{k=1}^{K} \alpha_k^c |\kappa_{lk} - \kappa_{mk}|$$

then we assume that the portion of the jump $1/2(U_{j+1} - U_{j-1})$ corresponding to

$$\alpha_l^c r_l + \alpha_m^c r_m \tag{3.4}$$

involves an eigenvector deficiency. Again we have set $c = 0.1$ for all of the computations presented here.

To guarantee that the slope-limiting procedure does not introduce instabilities into the computation of left and right states, it is necessary to guarantee that the entire jump corresponding to (3.4) is treated as one wave because the individual components of the jump are, in general, badly behaved as a result of the ill-conditioning of the matrix associated with the expansion. More precisely, we want to reduce α_l^c and α_m^c by the same multiplicative factor and force the two components of the wave to travel at the same speed. If $\lambda_l \lambda_m < 0$ then we simply set both of the amplitudes α_l^c and α_m^c to zero. If the waves speeds are of the same sign, we define an effective wave speed $\bar{\lambda}_{l,m} = \frac{1}{2}(\lambda_l + \lambda_m)$ to be used in computing left and right states for the flux computation. We also limit each component the same amount by defining $\omega_{l,m} = \alpha_{l,m}/\alpha_{l,m}^c$ and redefining the limited slopes by setting

$$\bar{\alpha}_{l,m} = \min(\omega_l, \omega_m)\, \alpha_{l,m}^c.$$

Using these definitions we define $(\Delta U)_j$ in Eq. (3.1) by

$$(\Delta U)_j = \sum \alpha_k r^k. \tag{3.5}$$

We now use the slopes defined by (3.5) to compute time-centered left and right states at the cell edges. Values in cell Δ_j are used to compute $U_{j+1/2}^{n+1/2,\mathrm{L}}$ and $U_{j-1/2}^{n+1/2,\mathrm{R}}$. The computation is based on a Taylor series expansion about the cell center, using the quasilinear form of the equation to replace temporal derivatives of U. For the left state we have, to the required order of accuracy,

$$\begin{aligned} U_{j+1/2}^{n+1/2,\mathrm{L}} &= U_j^n + \frac{\Delta x}{2} U_{x,j} + \frac{\Delta t}{2} U_{t,j} \\ &= U_j^n + \frac{\Delta x}{2} U_{x,j} - \frac{\Delta t}{2} F_{x,j} \\ &= U_j^n + \left(\frac{\Delta x}{2} - \frac{\Delta t}{2} DF\right) U_{x,j}. \end{aligned} \tag{3.6}$$

For linear problems, Eq. (3.6) can be used to compute left and right states by replacing U_x with the approximation (3.1). However, for nonlinear problems we modify (3.6) to disregard components in U_x corresponding to waves that do not propagate towards the cell edge. To eliminate these components we define the characteristic projection operators

$$P^{\pm} = R\Lambda^{\pm}R^{-1},$$

where R is the matrix whose columns are the r_k and $\Lambda^{\pm}$ is a diagonal matrix with $\Lambda^{\pm}_{kk} = \frac{1}{2} \pm \frac{1}{2}\,\mathrm{sign}(\lambda_k)$. (For both operators we use a diagonal entry of one for $\lambda_j = 0$.) Then,

$$U^{n+1/2,\mathrm{L}}_{j+1/2} = U^n_j + \tfrac{1}{2}P^+\left(I - \frac{\Delta t}{\Delta x}\,DF_j\right)\Delta U_j$$

$$U^{n+1/2,\mathrm{R}}_{j-1/2} = U^n_j - \tfrac{1}{2}P^-\left(I + \frac{\Delta t}{\Delta x}\,DF_j\right)\Delta U_j.$$

We note that the treatment of slopes near eigenvector deficiencies was specifically designed to avoid any difficulties arising in the computation of the left and right states because of ill-conditioning of DF or the projection operators.

We now evaluate the numerical flux corresponding to these left and right states using the procedures described in Section 2. For the higher order scheme, we modify the flux by adding a quadratic artificial viscosity. Thus

$$\tilde{F}_{j+1/2} = F^S(U^{n+1/2,\mathrm{L}}_{j+1/2},\, U^{n+1/2,\mathrm{R}}_{j+1/2}) - v_{j+1/2}(U^n_{j+1} - U^n_j), \tag{3.7}$$

where $v_{j+1/2} = c\,\max_k(\lambda_{k,j} - \lambda_{k,j+1}, 0)$. (Once again we set $c = 0.1$.) The addition of this artificial viscosity term adds a dissipation term to prevent the formation of steady discontinuities that fail to satisfy the Oleinik–Liu entropy conditions. Finally, the numerical fluxes defined by (3.7) are used in the conservative difference formula (2.2) to update the cell averages.

4. Numerical Examples for Model Problems

In the previous sections we developed the higher order Godunov scheme for general hyperbolic systems of conservation laws. In this section we validate the method by applying it to two model problems for which analytic solutions are known. For each model, we discuss the characteristic structure that is needed for the algorithm and present numerical examples. In the next section we apply the method to a problem of greater physical interest.

4.1. *Polymer Flood Model*

The first of our model problems is originally due to Keyfitz and Kranzer [8] and describes the transverse and longitudinal vibrations of a string. This model has the

same structure as a simple model for a polymer flood described by Pope [22] and analyzed by Isaacson [23]. The phase space for this model contains one or more curves along which both the wave speeds coincide and there is an eigenvector deficiency in the linearized coefficient matrix. There are also local linear degeneracies in one of the wave modes.

In our discussion we will use the polymer-flood model. This system describes the flow in a porous medium of a two-phase, incompressible fluid consisting of oil, water, and polymer. With suitable assumptions about flow geometry and boundary conditions the flow equations reduce to a system of two conservation laws with

$$U = \begin{bmatrix} s \\ cs \end{bmatrix}, \qquad F = \begin{bmatrix} v \\ cv \end{bmatrix}.$$

Here s is the volume fraction of aqueous phase, c is the concentration of polymer in the aqueous phase, and v is the phase velocity of water. The variables c and s have values between 0 and 1, and v is a given function of c and s.

The determination of the characteristic structure of this system is straightforward. The matrix of eigenvalues of $\partial F/\partial U$ is

$$\Lambda = \begin{bmatrix} \partial v/\partial s & 0 \\ 0 & v/s \end{bmatrix} = \begin{bmatrix} \lambda_1 & 0 \\ 0 & \lambda_2 \end{bmatrix}$$

and the matrix of right-eigenvectors is

$$R = \begin{bmatrix} 1 & \partial v/\partial c \\ c & c(\partial v/\partial c) + s(\lambda_2 - \lambda_1) \end{bmatrix}.$$

Note that when $\lambda_1 = \lambda_2$ the matrix R is singular indicating that there is an eigenvector deficiency.

Our numerical method also requires the gradients of the characteristic speeds. These are given by

$$\nabla_u \lambda_1 = \frac{1}{s}\left[\frac{\partial^2 v}{\partial s^2} s - \frac{\partial^2 v}{\partial s\, \partial c} c, \frac{\partial^2 v}{\partial s\, \partial c}\right]$$

and

$$\nabla_u \lambda_2 = \frac{1}{s^2}\left[(\lambda_1 - \lambda_2)\, s - \frac{\partial v}{\partial c} c, \frac{\partial v}{\partial c}\right].$$

From the latter equation, it is easy to see that the second eigenvalue is linearly degenerate. Furthermore, it is not hard to see that c is the Riemann invariant corresponding to λ_1. In fact, c is also invariant on the Hugoniot loci for the first wave family.

We describe three numerical computations with this model. For these computations we used

$$v(s, c) = \frac{s^2}{0.35(\frac{1}{2}+c)}\left[v_t + g\frac{(1-s)^2}{0.35}\right] \Big/ \left(\frac{s^2}{0.35(\frac{1}{2}+c)} + \frac{(1-s)^2}{0.35}\right),$$

where v_t and g are constants representing total flow velocity and gravity. Our first example is a gravity-inversion problem in which a heavy fluid is placed above a light fluid. We take $v_t = 0$ and $g = -1.4$. The initial data are $c = 0.1$ and $s = 0.1$ for $x < 0$ and $c = 0.9$ and $s = 0.95$ for $x > 0$. Computational results with 100 and 200

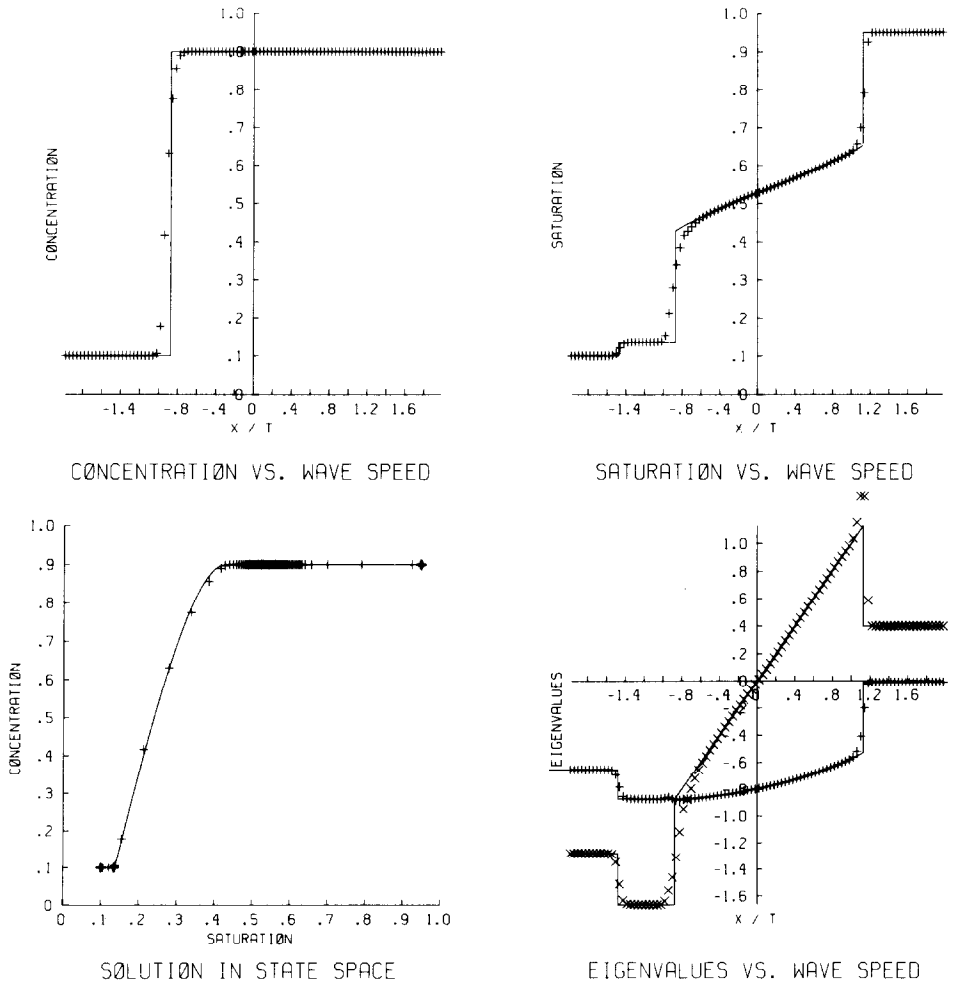

FIG. 1. Polymer flood gravity inversion example using 100 cells.

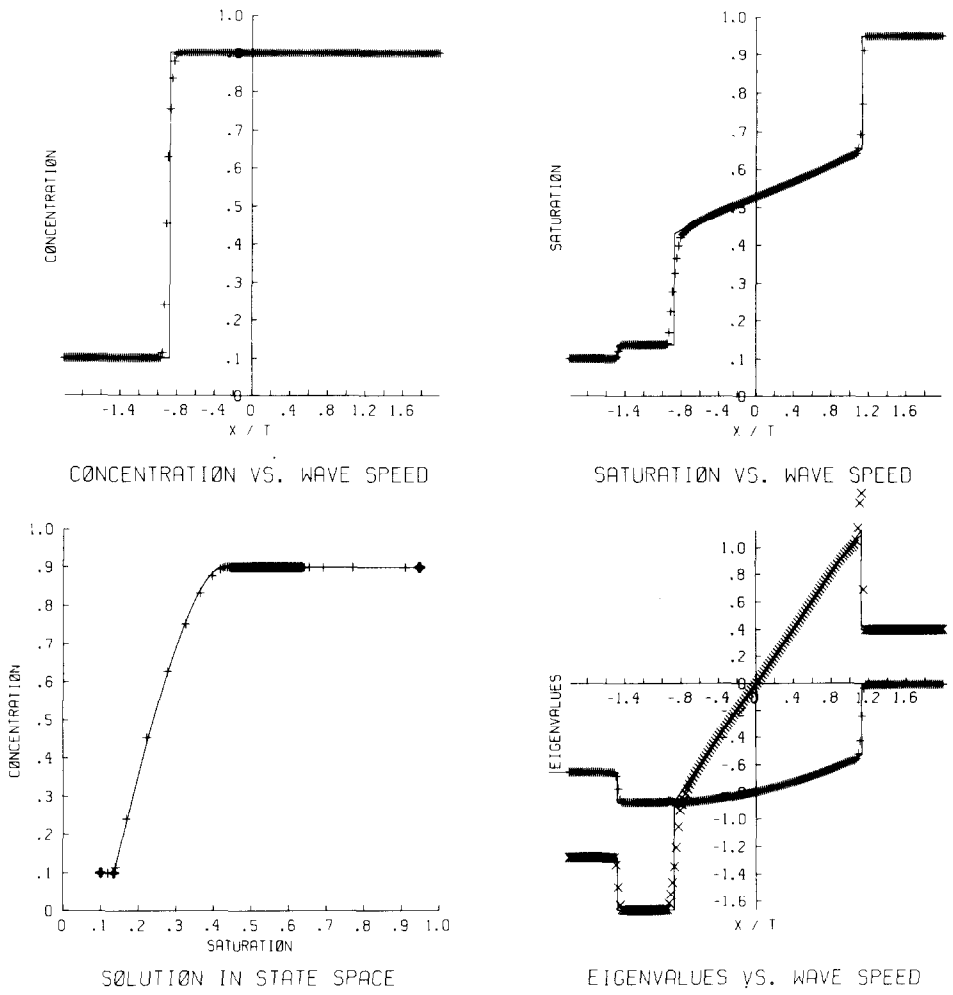

FIG. 2. Polymer flood gravity inversion example using 200 cells.

and 200 steps, respectively, with $\Delta t/\Delta x = 0.25$. In addition to plotting c and s versus x/t, we also plot the solution in phase space and eigenvalues versus x/t. The analytic solution (drawn with solid lines) consists of a shock moving rapidly to the left, separated by a constant state from a compound wave consisting of a contact discontinuity moving to the left, a transonic rarefaction and a shock moving to the right. Just to the right of the contact discontinuity there is a loss of strict hyperbolicity. Note that there is good agreement of both computations to the analytic solution and that the solution demonstrates convergence as the mesh is refined. The spike in the numerical wave speeds at $x/t = 1.1$ is a characteristic signature of a local linear degeneracy arising because the smeared shock passes through a region of phase-space in which the wave speed is higher than the shock-speed.

To provide a more difficult test for the numerical method we would like to have a stationary eigenvector deficiency. Unfortunately, this does not occur for any values of v_t and g. To devise such a test we have used a horizontal reservoir ($v_t = 1$ and $g = 0$) and performed the computation in a moving frame of reference so that both wavespeeds are equal when they are zero. These results for 100 and 200 cells (100 and 200 steps, respectively, with $\Delta t/\Delta x = 0.5$) are shown in Figs. 3 and 4. Here, the fluid on the left has $c = 0.9$ and $s = 1.$, while the fluid on the right has $c = 0.1$ and $s = 0.1$. The analytic solution consists of a shock moving to the right, separated by a constant state from a compound wave consisting of a sonic contact discontinuity and a rarefaction moving to the left. Again, the analytic solution is drawn in these figures with a solid line. Note that in this case there is a slight phase shift in the numerical solution; however, convergence is still observed.

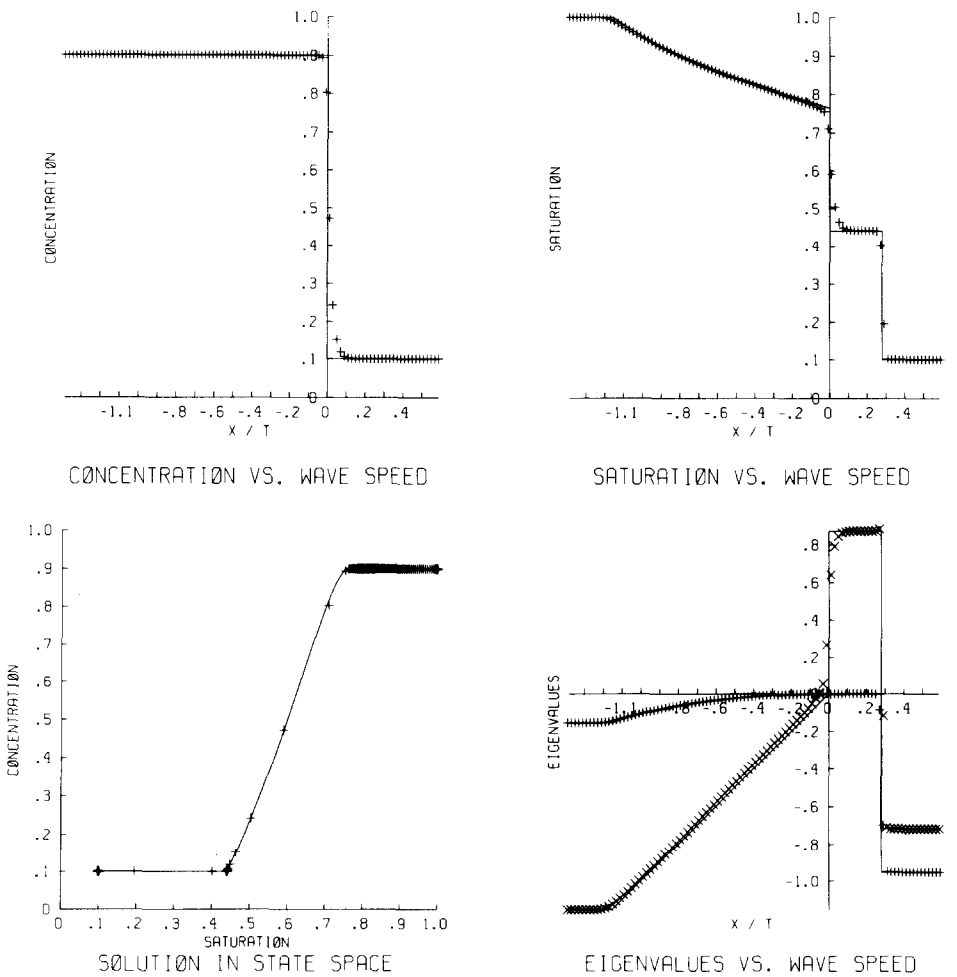

FIG. 3. Polymer flood on moving grid using 100 cells.

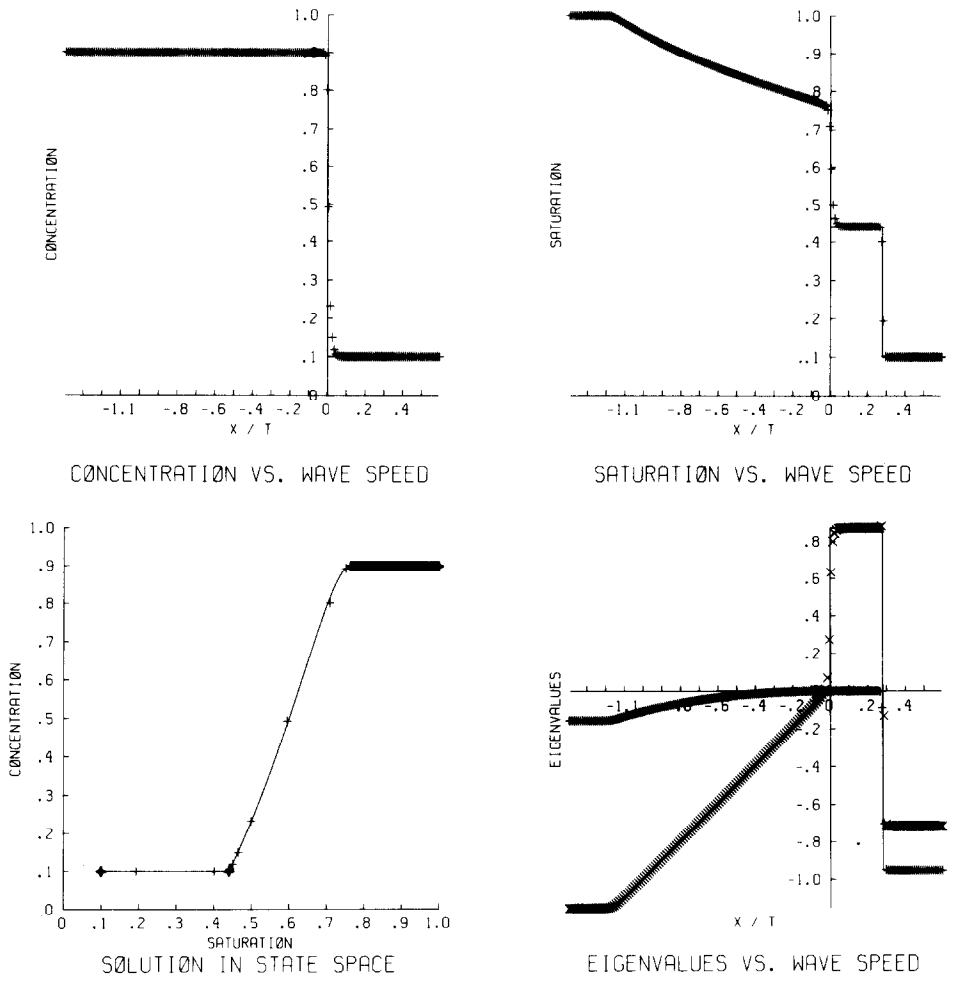

FIG. 4. Polymer flood on moving grid using 200 cells.

In our third numerical example for the polymer flow model, the initial data were chosen so that both of the characteristic speeds were equal everywhere. The computation was performed with 200 grid cells. Cells 2 through 26 were taken to have compositions varying smoothly between those in cells 1 and cells 27–200, and to have both wavespeeds equal. The numerical results in Fig. 5 (plotted as a continuous line) show that the large-time behavior of this problem is distinct from the solution to the Riemann problem between the left and right states. Furthermore, note that the nonlinearities in the problem have driven the solution off of the degeneracy curve, as observed by Isaacson [23]. This supports our assumption in the Introduction that the loss of strict hyperbolicity is confined to a region of codimension $\geqslant 1$ in space-time.

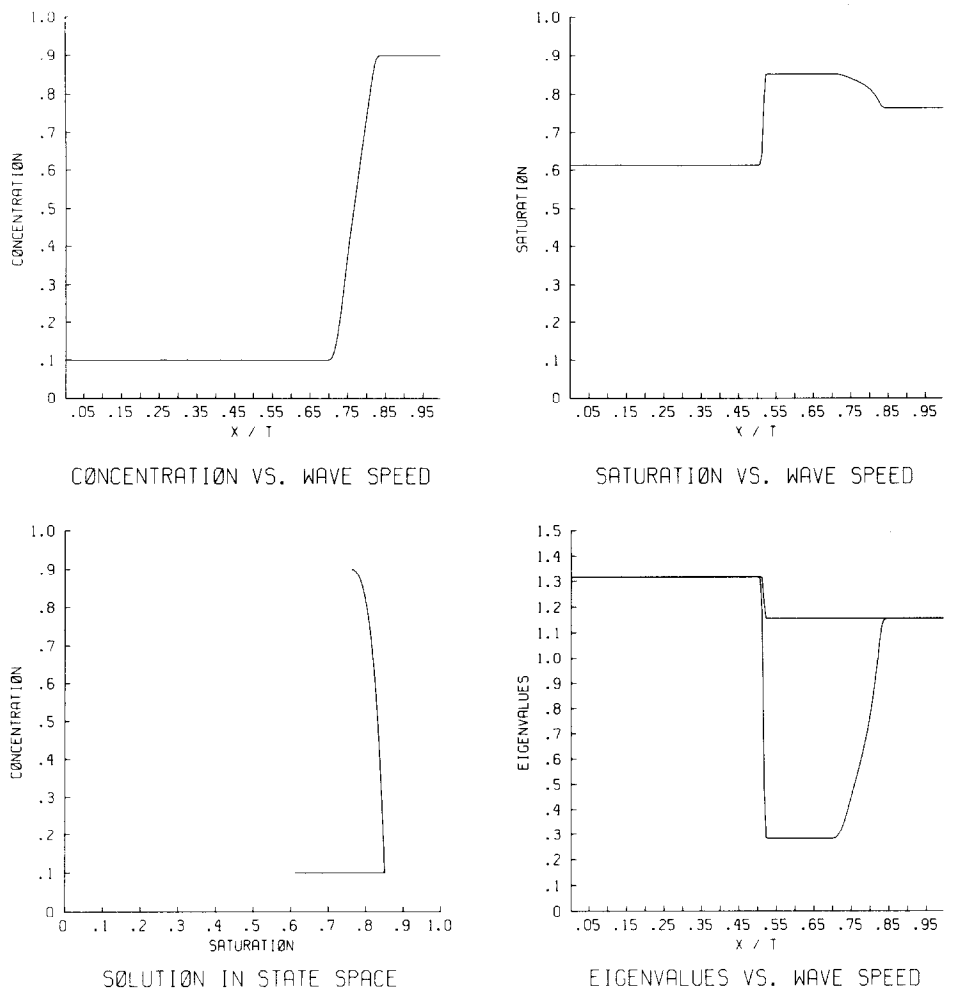

FIG. 5. Polymer flood with data on eigenvector deficiency curve.

4.2. *Complex Burgers' Equation*

The second model problem is the complex Burgers' equation described by Shearer *et al.* [24]. Unlike the previous model, this conservation law has a single point at which strict hyperbolicity fails. However, the presence of this "umbilic point" leads to undercompressive shocks, for which exactly one characteristic intersects the shock on either side.

This conservation law can be written in the form

$$\frac{\partial z}{\partial t} - \frac{\partial \bar{z}^2}{\partial x} = 0,$$

where z is the complex variable

$$z = u_1 + iu_2 = \rho e^{i\theta}.$$

From this form of the equation, it is easy to see that the conservation law is unaffected by conjugation (i.e., reflection about the u_1 axis), and clockwise or counterclockwise rotations of 120°. This conservation law can be written in the form (2.1) if we take

$$U = \begin{bmatrix} u_1 \\ u_2 \end{bmatrix} = \begin{bmatrix} \cos\theta \\ \sin\theta \end{bmatrix} \rho$$

and

$$F = \begin{bmatrix} u_2^2 - u_1^2 \\ 2u_1 u_2 \end{bmatrix} = \begin{bmatrix} -\cos 2\theta \\ \sin 2\theta \end{bmatrix} \rho^2.$$

In order to perform the characteristic analysis of this conservation law, let us define

$$W = \begin{bmatrix} \rho \\ \theta \end{bmatrix}.$$

Then the quasi-linear form of the conservation law for W shows that the equation is hyperbolic if and only if the eigenvalues of

$$A = \left[\frac{\partial U}{\partial W}\right]^{-1} \frac{\partial F}{\partial W} = \begin{bmatrix} 1 & 0 \\ 0 & \rho \end{bmatrix}^{-1} \begin{bmatrix} -\cos 3\theta & \sin 3\theta \\ \sin 3\theta & \cos 3\theta \end{bmatrix} \begin{bmatrix} 1 & 0 \\ 0 & \rho \end{bmatrix} 2\rho$$

are real. Since A is similar to a symmetric orthogonal matrix it has real eigenvalues given by the diagonal entries of the matrix

$$\Lambda = \begin{bmatrix} -2\rho & 0 \\ 0 & 2\rho \end{bmatrix}$$

and right eigenvectors given by the columns of

$$X = \begin{bmatrix} 1 & 0 \\ 0 & \rho \end{bmatrix}^{-1} \begin{bmatrix} -\cos\frac{3}{2}\theta & \sin\frac{3}{2}\theta \\ \sin\frac{3}{2}\theta & \cos\frac{3}{2}\theta \end{bmatrix}.$$

In order to find the characteristic directions of the original form of the conservation law, we note that

$$\frac{\partial F}{\partial U} = \frac{\partial U}{\partial W} A \left[\frac{\partial U}{\partial W}\right]^{-1}.$$

Thus the desired characteristic directions are the columns of

$$R = \frac{\partial U}{\partial W} X = \begin{bmatrix} -\cos\frac{\theta}{2} & \sin\frac{\theta}{2} \\ \sin\frac{\theta}{2} & \cos\frac{\theta}{2} \end{bmatrix}.$$

Note that these characteristic directions are orthogonal and undefined at the origin. Also note that the gradients of the eigenvalue are easy to compute,

$$\frac{\partial 2\rho}{\partial U} = \frac{2}{\rho} u^{\mathrm{T}} = 2[\cos\theta, \sin\theta],$$

but they are undefined at the origin.

We can use these forms of the characteristic directions to find the Riemann invariants (although the Riemann invariants are not used by our numerical method). The Riemann invariant corresponding to the positive wavespeed must have its gradient in the direction of the first left eigenvector; in other words,

$$\frac{\partial \omega}{\partial W} = \alpha e_1^{\mathrm{T}} X^{-1} = \alpha \left[-\cos\tfrac{3}{2}\theta, \rho \sin\tfrac{3}{2}\theta \right]$$

for some scalar α. It is now easy to see that this Riemann invariant is

$$\omega = \rho^{3/2} \cos\tfrac{3}{2}\theta = \mathrm{Re}\,(z^{3/2})$$

The other Riemann invariant, corresponding to the negative wavespeed, is

$$\omega = \rho^{3/2} \sin\tfrac{3}{2}\theta = \mathrm{Im}(z^{3/2}).$$

The rarefaction curves lie on the level sets of these Riemann invariants, and therefore, asymptote to infinity whenever the sines or cosines approach zero. Since the characteristic speeds are proportional to the distance of the points on these level sets from the origin, the wave families are not genuinely nonlinear.

We perform a numerical calculation with this model primarily to investigate the behavior of our method on problems containing undercompressive shocks. We chose the Riemann problem initial data with left state $U = [\cos(\pi/6), \sin(\pi/6)]$, and the right state its negative. The choice of symmetric states leads to a sonic undercompressive shock which is the most difficult case for the numerical method. The analytic solution consists of forward- and backward-moving rarefactions and a sonic undercompressive shock. Figure 6 shows the results of our numerical method with 100 grid cells. The analytic solution as determined in [24] is drawn with a solid line. There is excellent agreement between the analytic and numerical solution. Other examples have further corroborated the agreement between the results of our

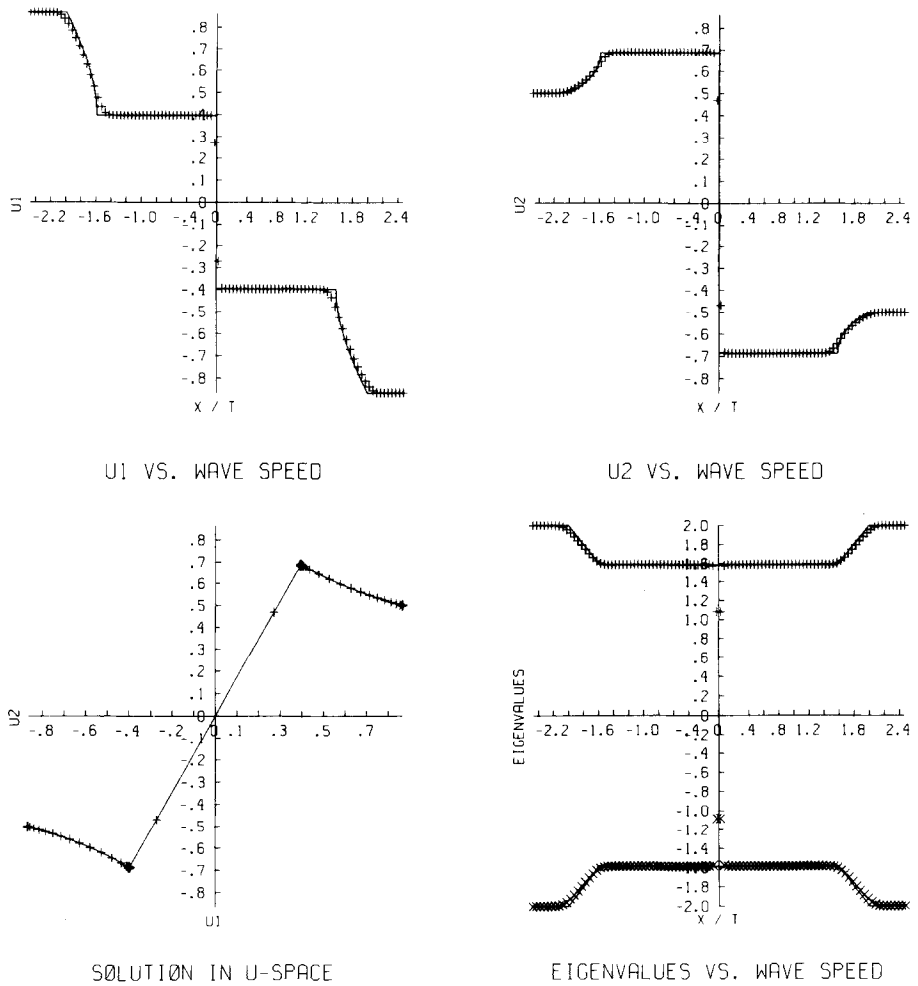

FIG. 6. Complex Burger's equation with sonic undercompressive shock using 100 cells.

5. BLACK-OIL MODEL

In our previous numerical examples we examined non-strictly hyperbolic conservation laws for which there are known solutions to the Riemann problems. In this section we apply the methodology to a problem of practical interest, namely, the black-oil model for petroleum reservoir simulation. The black-oil model is the standard model used in petroleum engineering to simulate primary and secondary oil recovery processes. It is able to model a variety of effects including fluid compressibility and the transfer of chemical components between phases. Unfortunately, the black-oil model is too intricate to discuss fully in this paper. We will give only

a brief synopsis of the equations. The details of the model and an analysis of its structure are described in [25].

Analytic Structure

The black-oil model describes a three component fluid system (oil, gas, and water) and may contain up to three fluid phases (liquid, vapor, and aqua). The other dependent variable used to describe the system is the pressure. Because of the transfer of chemical components between phases, it is possible that for certain compositions and pressures a phase may not be formed even though all three chemical components are present. When all three phases are present the fluid is said to be saturated; when one of the phases is missing the fluid is said to be undersaturated.

The flow equations describing the system, which express conservation of mass for each chemical component, take the form

$$\frac{\partial n\phi}{\partial t} + \nabla \cdot F(n, p, v) = 0, \tag{5.1}$$

where n is the vector of component densities, p is the pressure, v is the vector of phase velocities, and ϕ is the porosity of the porous medium. Darcy's law specifies $v = v(p, \nabla p, n, s)$, where s is the vector of phase saturations which are expressed as functions of p and n. The system is closed by an equation of state for the fluid mixture

$$V(p, n) = 0. \tag{5.2}$$

The system (5.1) and (5.2) have a number of properties that are important in the design of numerical solution algorithms. At the boundaries of regions where the fluid changes from being saturated to being undersaturated the flux F is continuous but its derivative is not. Also, the system (5.1)–(5.2) is of indeterminate type; it exhibits both hyperbolic and parabolic behavior. Trangenstein and Bell [25] define a decomposition of the system that separates the parabolic and hyperbolic character of the flow. In particular they define a parabolic pressure equation of the form

$$a\frac{\partial p}{\partial t} - \nabla \cdot (b \nabla p) = c(p, n, \nabla p), \tag{5.3}$$

where the coefficients a and b are functions of n and p. In addition to determining p, the result of the pressure equation is also used to define a total fluid velocity v_t. Then, (5.1) can be rewritten in the form

$$\frac{\partial n\phi}{\partial t} + \nabla \cdot \bar{F}(n, p, \tilde{v}) = 0, \tag{5.4}$$

where $\tilde{v} = \tilde{v}(p, v_t, n, s)$ is the vector of phase velocities expressed in terms of total velocity. If we treat p and v_t as known functions of x, t then (5.4) is hyperbolic.

Next we summarize the resuls of the characteristic analysis of (5.4) from [25]. The actual form of $\bar{F}$ (and F) changes at phase boundaries. For this reason the

characteristic structure of (5.4) changes depending on whether the fluid is saturated or undersaturated.

In the saturated case, the characteristic speeds are of two types. One wavespeed is identically zero. Its Riemann invariant is related to the error in (5.2) introduced by decoupling the flow equations; ideally, this wave carries no information. The remaining characteristic speeds are eigenvalues of $\partial\tilde{v}/\partial s$. These wavespeeds exhibit several forms of difficult behavior. Two wavespeeds can become equal at isolated points or along curves extending to the boundary of the saturated region. Each wave family also exhibits local linear degeneracies. Further, there is no consistent global ordering of these two eigenvalues that gives a smooth family of eigenvectors.

In the undersaturated case, the characteristic speeds are of three types. There is a zero wavespeed carrying essentially no information, just as in the saturated case. The second wavespeed is the derivative of the velocity of the aqueous phase with respect to its saturation. The wave curves for this family contain points of local linear degeneracy. The third wavespeed is a weighted average of the particle velocities in the existing phases, and is essentially linearly degenerate. (The particle velocity for a phase i is v_i/s_i.) Thus the structure of the undersaturated case is similar to the polymer flood model. In particular, there is an eigenvector deficiency whenever the second and third eigenvalues are equal.

A number of remarks regarding the characteristic structure are in order. First, the discontinuity in the derivative of the flux at phase boundaries leads to a discontinuity in both the characteristic speeds and the associated right eigenvectors. Also, because of the complexity of the formulae for the eigenvalues, we have not attempted to analytically compute the structure coefficients required by our numerical method. In the numerical resuls below, the structural coefficients have been computed by finite differences from analytic calculations of the characteristic speeds and directions.

Numerical Considerations

Equations (5.3) and (5.4) form the basis for a numerical method in which we first solve (5.3) to determine p and v_t, and then use these functions to solve (5.4) for n. In solving (5.3) we add an additional source term to correct for errors introduced by the sequential solution scheme. The additional complexity of the black-oil model necessitates additional modifications to the Godunov methodology. First, the quasilinear form of the equation used to predict left and right states for the flux computation contains additional terms arising from the dependence of the flux on pressure and total velocity. Precisely, the quasilinear form (in one space dimension) is given by

$$\phi\frac{\partial n}{\partial t}+\left(\frac{\partial F}{\partial n}+\frac{\partial F}{\partial \tilde{v}}\left(\frac{\partial \tilde{v}}{\partial n}+\frac{\partial \tilde{v}}{\partial s}\frac{\partial s}{\partial n}\right)\right)\frac{\partial n}{\partial x}$$
$$=-\left(\frac{\partial F}{\partial p}+\frac{\partial F}{\partial \tilde{v}}\left(\frac{\partial \tilde{v}}{\partial p}+\frac{\partial \tilde{v}}{\partial s}\frac{\partial s}{\partial p}\right)\right)\frac{\partial p}{\partial x}-\frac{\partial F}{\partial \tilde{v}}\frac{\partial \tilde{v}}{\partial v_t}\frac{\partial v_t}{\partial x}$$

The terms appearing on the right-hand side of this equation are source terms that must be included in (3.6) to obtain second-order accuracy.

The other modification to the Godunov methodology is required because of the discontinuity of the eigenstructure. At interfaces of cells containing different phases, the discontinuity in the flux derivatives means that the phase-space construction for weak waves in Section 2 is invalid for part of the jump. This can be alleviated by addition of a quadratic viscosity to the flux based on the maximum saturation jump. In particular, we modify the viscosity term in (3.7) to

$$\bar{v}_{j+1/2} = \max(v_{j+1/2}, 0.2\Delta x\, \Delta s^m_{j+1/2}/\Delta t),$$

where

$$\Delta s^m_{j+1/2} = \begin{cases} \max_i |s_{j,i} - s_{j+1,i}| & \text{if } \max_i |s_{j,i} - s_{j+1,i}| > 0.2 \\ 0 & \text{otherwise.} \end{cases}$$

Computational Examples

We describe two black-oil computational examples. The explicit functional forms used for the function defining the model are too complex to be presented here; the computations were all performed using the data in [25]. The first example is a 1-dimensional gravity inversion problem. The porous medium is 100 ft in length (vertical) and is capped with no flow boundary conditions at each end. The lower third is initially filled with pure gas, the middle third with pure oil, and the upper third with pure water. The pressure throughout the medium is initially 2000 psi. When allowed to flow, the fluids begin to invert because of gravity and to mix because of mass transfer. The mass transfer effects are quite substantial. A large fraction of the gas component is absorbed into the liquid phase resulting in a pressure drop of more than 30% in the first 200 days of the simulation. In Fig. 7, 8, and 9 we plot computation results at 120 days with 60, 120, and 240 cells. The left side of the plot corresponds to the bottom of the domain. In each case we plot the saturations and the eigenvalues. In the saturation plot, the area below the lower curve represents, the vapor phase saturation, the area between the lower and upper curve is the liquid saturation, and the area above the upper curve is the aqueous saturation. The three different grids serve to illustrate the resulution capability of the method and to demonstrate numerical convergence of the solution. In the two coarser grids we identify the values of the solutions at the cell centers with plus symbols; for clarity, we omit these symbols in the fine grid calculation. Examining the results more closely, we see that the solution at 120 days consists of two compound waves emanating from the discontinuities in the original data. Each compound wave consists of a shock-rarefaction pattern. These two waves demonstrate somewhat different phenomena in that there is a phase change across the two shocks in the lower wave but not in the upper wave. The wave speed plots for these computations provide only qualitative information about the wave because they are constantly being modulated by pressure effects. In Figs. 7–9, we do observe that each of the shock waves shows the typical signature of local linear degeneracy, i.e.,

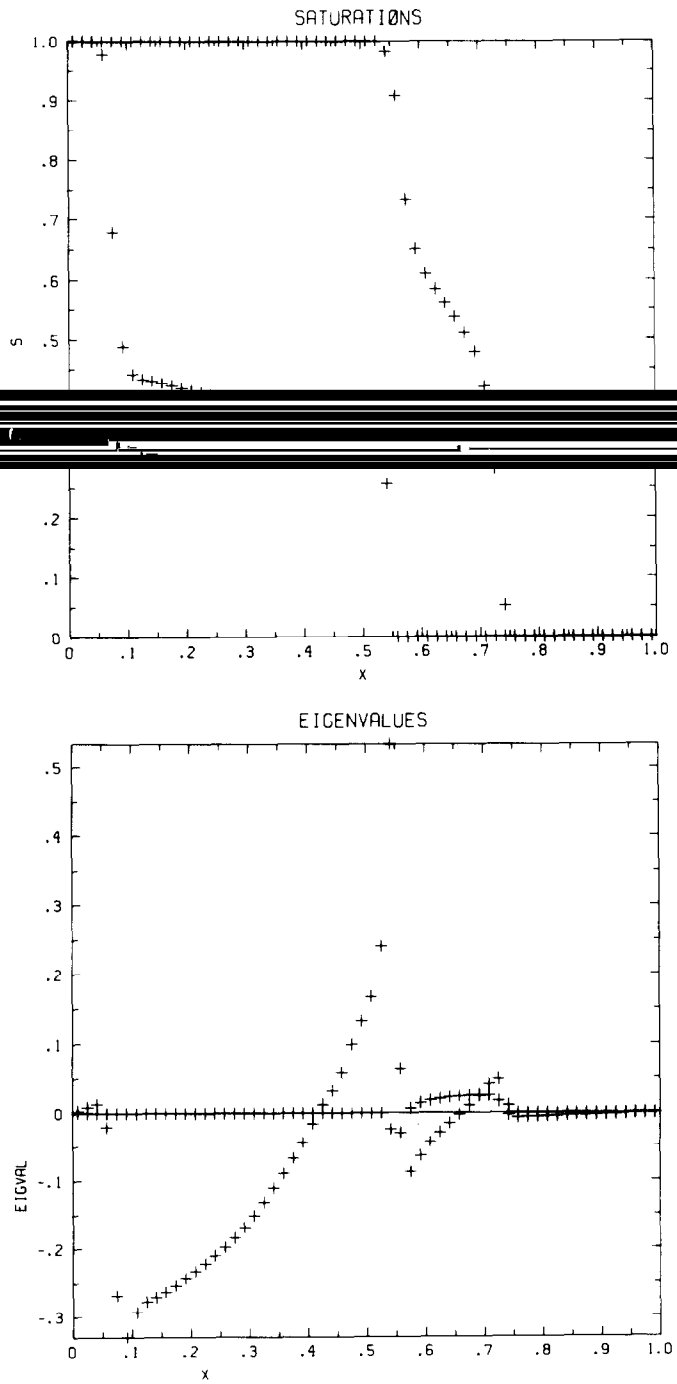

FIG. 7. Black-oil gravity inversion example with 60 cells at roughly 120 days.

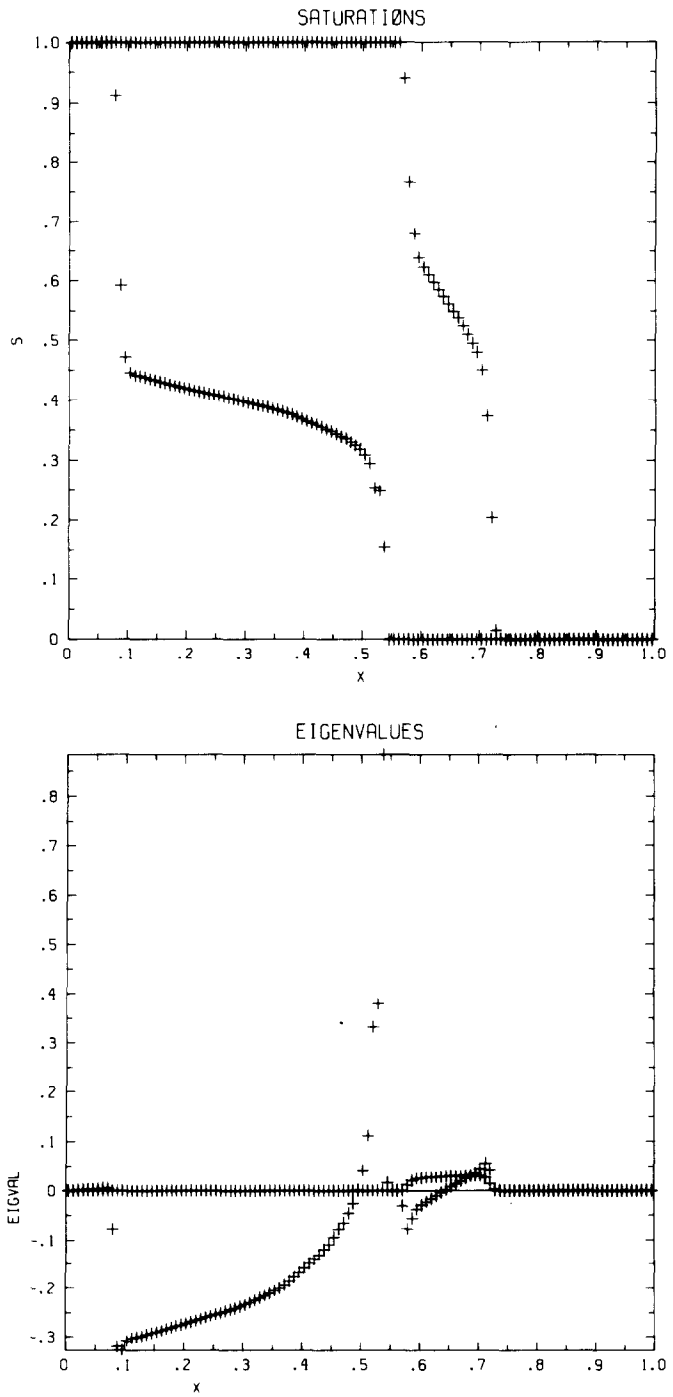

FIG. 8. Black-oil gravity inversion example with 120 cells at roughly 120 days.

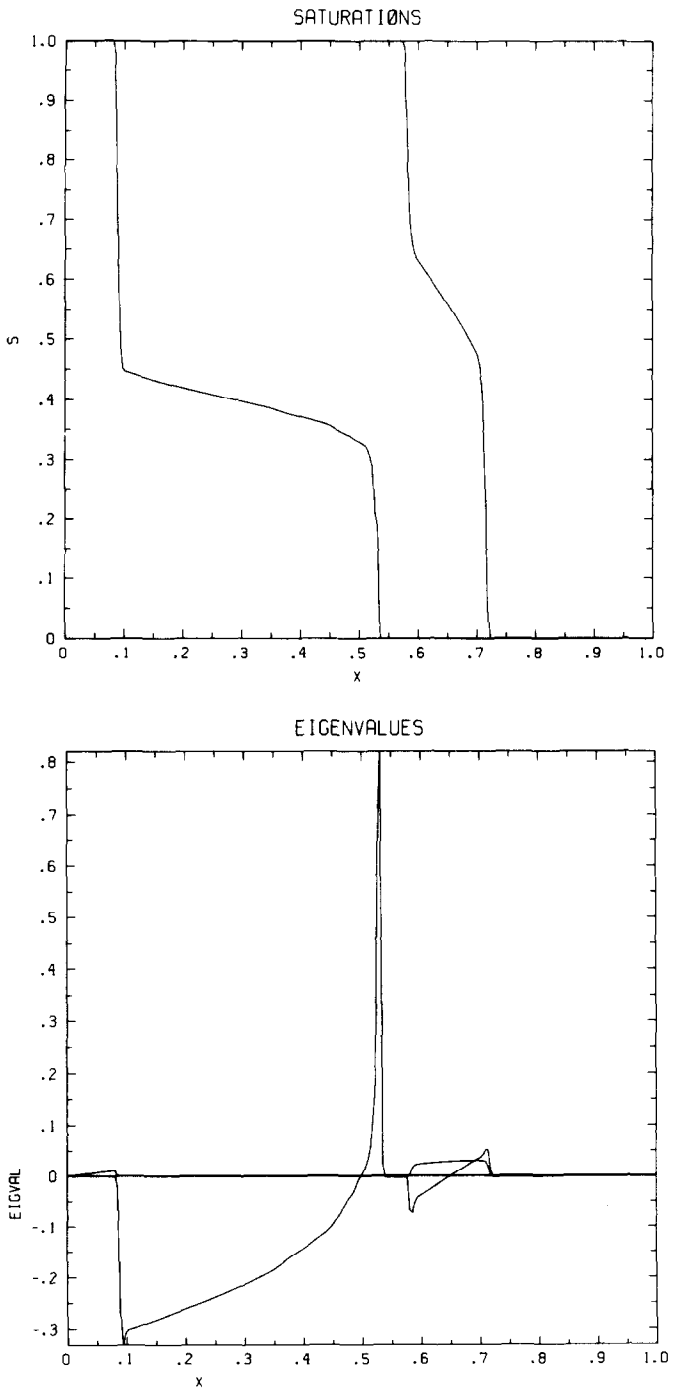

FIG. 9. Black-oil gravity inversion example with 240 cells at roughly 120 days.

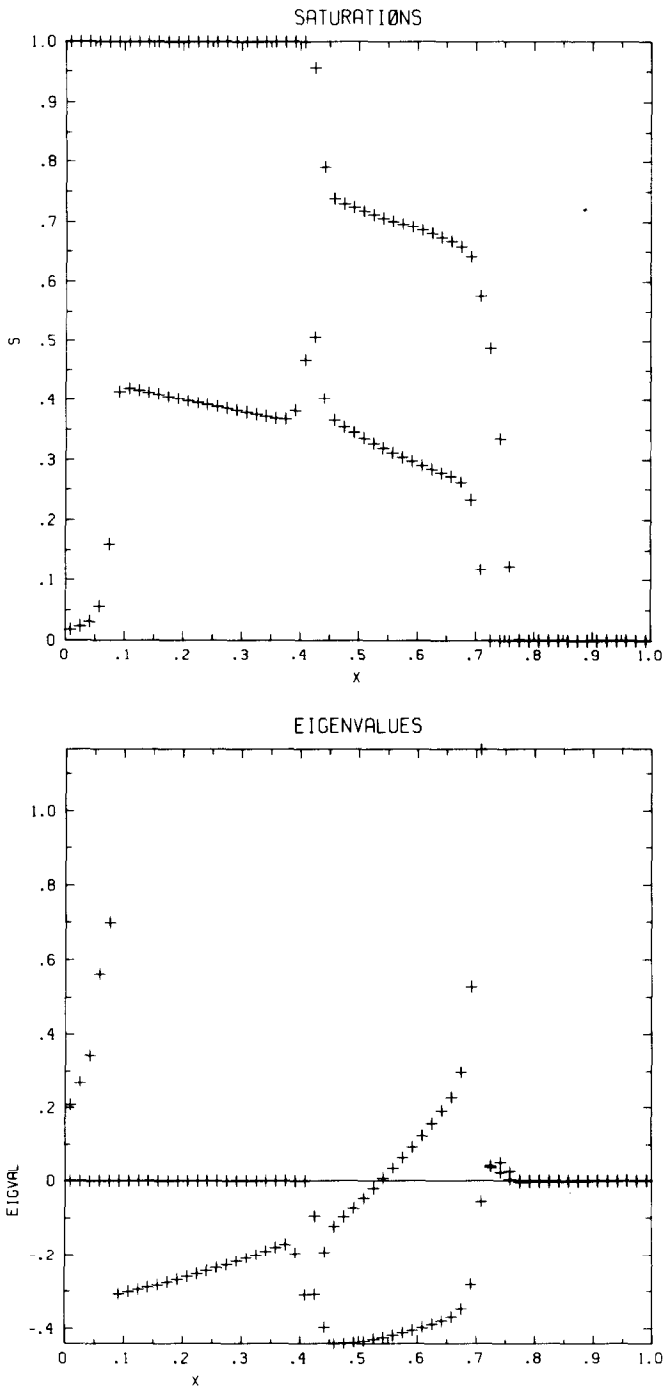

FIG. 10. Black-oil gravity inversion example with 60 cells at roughly 180 days.

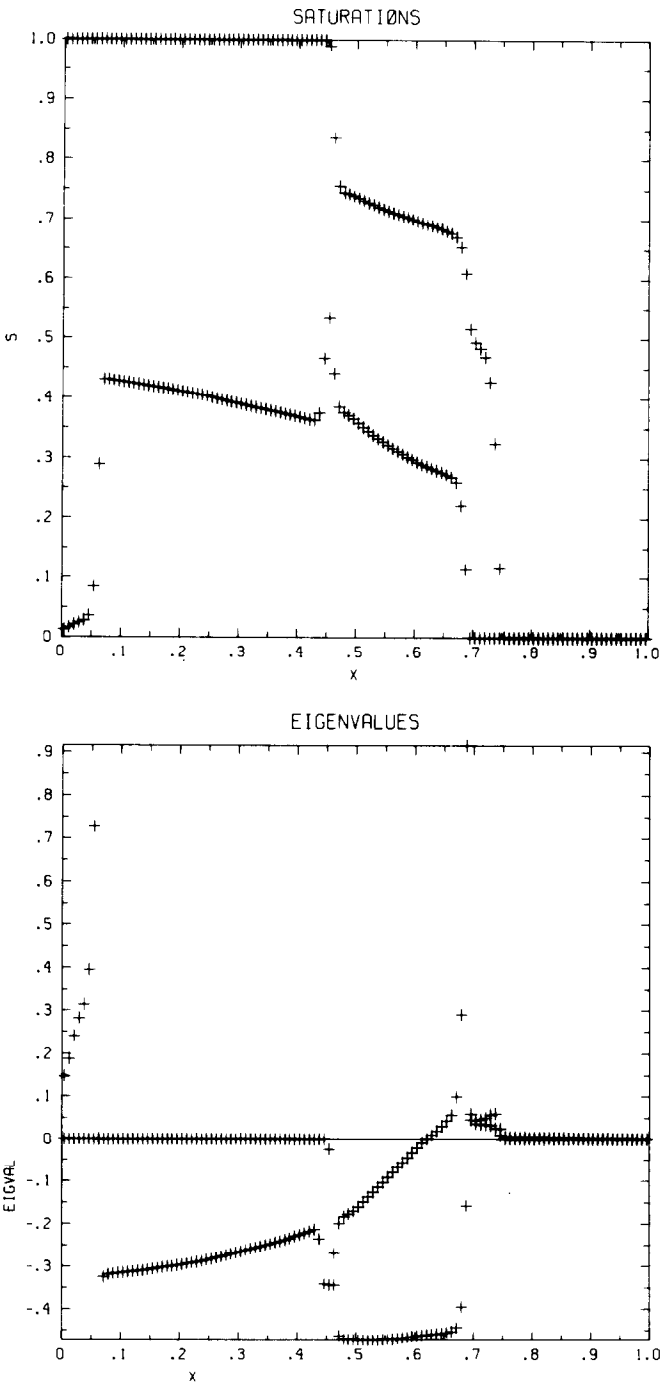

FIG. 11. Black-oil gravity inversion example with 120 cells at roughly 180 days.

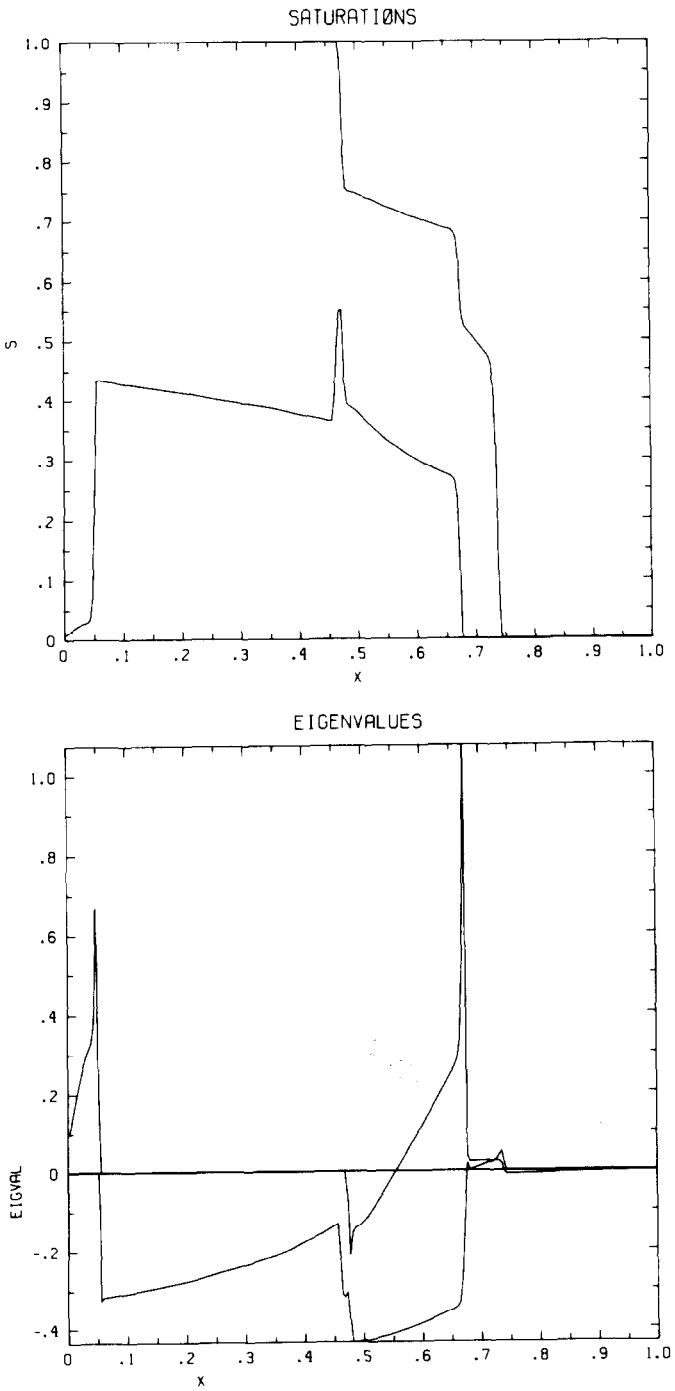

FIG. 12. Black-oil gravity inversion example with 240 cells at roughly 180 days.

a local spike in the wave speed. Furthermore, we can observe points where there is a loss of strict hyperbolicity as the wave speeds cross.

The next plots, Figs. 10, 11, and 12, show the interaction of the waves seen in the earlier figures. These plots show the solution at roughly 180 days for each of the three grids. Again, the refinements show convergence of the method. The solution is considerably more complex at this stage. A number of points of local linear degeneracy and loss of strict hyperbolicity are apparent. At $x = 0.05$ we see that the left-most front at 120 days has reached the bottom of the domain and has reflected back into the domain. Another feature of interest is the gas bubble that forms at the leading edge of the downward moving water front at $x = 0.55$.

The next example we consider is a 2-dimensional problem that is more typical of engineering computations. In this case the reservoir is 500 ft long and 50 ft thick with a uniform permeability of 100 md. The reservoir is initially filled with an undersaturated liquid phase containing oil and gas in hydrostatic equilibrium with mean pressure of 1800 psi. We inject pure water in hydrostatic equilibrium at mean pressure 2000 psi along the entire left face of the reservoir. Production occurs along the entire right face with bottom hole pressure of 1600 psi. The 2-dimensional scheme is a natural extension of the methods described earlier and the unsplit methodology developed by Colella [20]. For this case we plot, in Figs. 13–15, the component densities on 20×10, 40×20, and 80×40 grids after roughly one year of

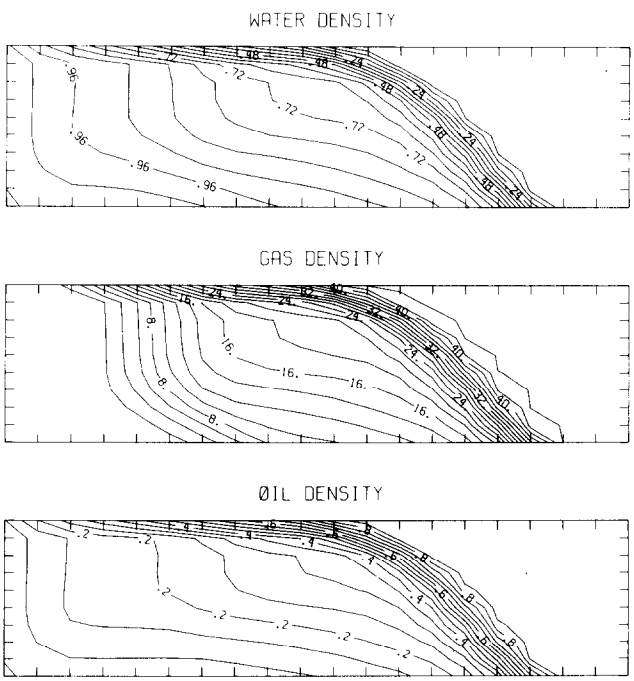

FIG. 13. Black-oil water-flood example on 20×10 grid at 360 days.

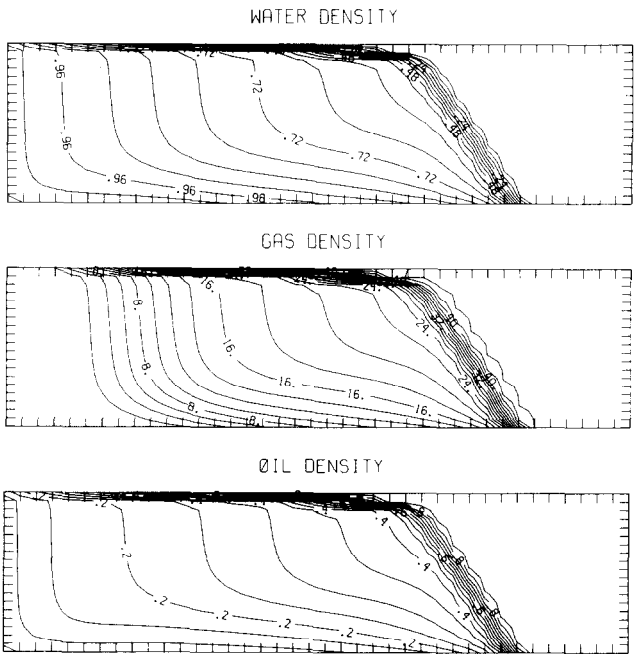

FIG. 14. Black-oil water-flood example on 40×20 grid at 360 days.

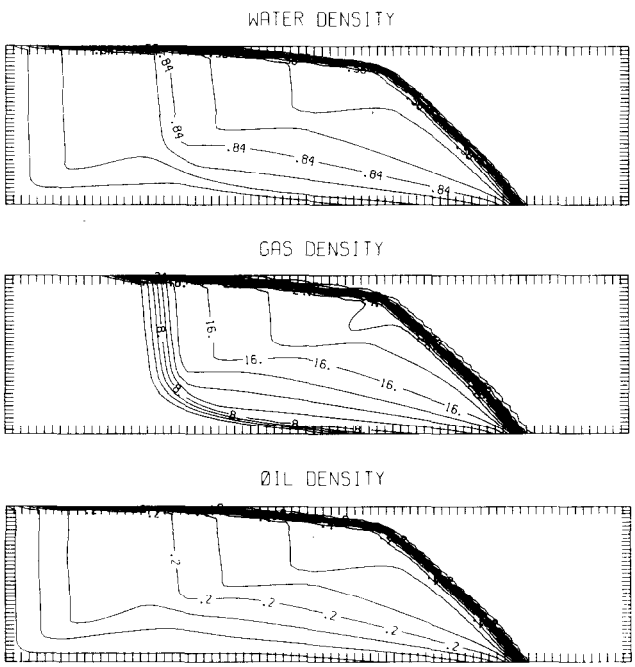

FIG. 15. Black-oil water-flood example on 80×40 grid at 360 days.

injection. The vertical dimension on the plots has been expanded by a factor of 2.5. We note that the aspect ratio of the grid cells is 5 to 1 for all of the computations. The width of the initial front is only a couple of cells wide on each of the grids. The flow also contains a number of secondary features that are quite difficult to resolve accurately. Along the top of the reservoir there is a liquid hydrocarbon "film" that is bypassed by the heavier injected water. Another interesting feature is the contact discontinuity seen in the leftmost contours of the gas density. The contact, which is smeared over 3–4 cells, is completely resolved only on the finest grid. To the left of this contact all of the gas is being swept from the liquid phase by the injected water.

6. Conclusions

Over the past few years we have seen the development of high-resolution schemes for hyperbolic conservation laws achieve an important milestone. The basic algorithm design principles needed to construct schemes for systems such as gas dynamics in which all wave modes are either genuinely nonlinear or linearly degenerate are now well understood. There are a number of methods that have been developed using these principles and they have all proven to be quite successful. One of the next major challenges facing algorithm designers is the extension of these methodologies to more general systems of equations. In this paper we have presented a prototype methodology for performing this extension. The method is based on an approximation of the phase-space solution of the Riemann problem for strictly hyperbolic systems, plus a generalization of the Engquist–Osher flux. We have also presented the necessary constructions that are needed to detect loss of strict hyperbolicity along with modifications to the method to handle it. Tests on simple model problems with known exact solutions have indicated good performance of the method. The method has also been applied to more realistic problems arising in a model for multiphase flow in porous media and has performed well for these more difficult problems. However, it should be emphasized that we do not consider the methods developed here to be the final resolution of the problems associated with solving general systems of conservation laws. On the contrary, the methodology that has been presented here is only an initial step in that direction. We believe that we have identified some of the key issues that must be addressed and have presented one option for dealing with them. Several variations, some of which were suggested in the text, are posssible and may be necessary in other contexts.

References

1. D. L. Book, *Finite-Difference Techniques for Vectorized Fluid Dynamics* (Springer-Verlag, New York, 1981).
2. P. R. Woodward and P. Colella, *J. Comput. Phys.* **54**, 115 (1984).

3. H. C. YEE, NASA TM-89464, NASA Ames Research Center, May 1987 (unpublished).
4. B. VAN LEER, *J. Comput. Phys.* **23** 276 (1971).
5. P. D. LAX, *Commun. Pure Appl. Math.* **10** 537 (1957).
6. S. OSHER, *SIAM J. Num. Anal.* **21**, 217 (1984).
7. T. P. LIU, *J. Differential Equations* **18**, 218 (1975).
8. B. L. KEYFITZ AND H. C. KRANZER, *Arch. Rat. Mech. Anal.* **72**, 220 (1980).
9. D. G. SCHAEFFER AND M. SHEARER, *Commun. Pure Appl. Math.* **40** 141 (1987).
10. P. L. ROE, *J. Comput. Phys.* **43**, 357 (1981).
11. P. COLELLA AND H. M. GLAZ, *J. Comput. Phys.* **59**, 264 (1985).
12. B. ENGQUIST AND S. OSHER, *Math. Comput.* **34**, 45 (1980).
13. B. ENGQUIST AND S. OSHER, *Math. Comput.* **36**, 321 (1981).
14. S. OSHER AND F. SOLOMON, *Math. Comput.* **38**, 339 (1982).
15. S. K. GODUNOV, *Math. Sb.* **47**, 271 (1959).
16. E. M. MURMAN AND J. D. COLE, *AIAA J.* **9**, 114 (1971).
17. P. D. LAX, *Hyperbolic Systems of Conservation Laws and the Mathematical Theory of Shock Waves* (SIAM, Philadelphia, 1973).
18. A. HARTEN AND P. D. LAX, *SIAM J. Num. Anal.* **18**, 289 (1981).
19. V. V. RUSANOV, *Zh. Vychisl. Mat. Fiz.* **1**, 267 (1961).
20. P. COLELLA, LBL-17023, Lawrence Berkeley Laboratory, May 1984 *J. Comput. Phys.*, in press.
21. J. B. BELL AND G. R. SHUBIN, "Higher-Order Godunov Methods for Reducing Numerical Dispersion in Reservoir Simulation," *Eight SPE Symposium on Reservoir Simulation*, Dallas, Texas, February 10–13, 1985.
22. G. A. POPE, *Soc. Pet. Eng. J.* **20**, 191 (1980).
23. E. L. ISAACSON, "Global Solution of the Riemann Problem for a Non-Stricly Hyperbolic System of Conservation Laws Arising in Enhanced Oil Recovery," preprint (unpublished).
24. D. G. SCHAEFFER, M. SHEARER, D. MARCHESIN, AND P. PAES-LEME, *Arch. Rat. Mech. Anal.*, in press.
25. J. A. TRANGENSTEIN AND J. B. BELL, *SIAM J. Appl. Math.*, in press.